

Rivulet evolution in gravity-driven thin-film flows

D. Slade*, S. Veremieiev*, Y.C. Lee** and P.H. Gaskell*
Corresponding author: mndsl@leeds.ac.uk

* School of Mechanical Engineering, University of Leeds, Leeds, LS2 9JT, UK

** Department of Mechanical Engineering, Heriot-Watt University,
Edinburgh, EH14 4AS, UK

Abstract: The evolution of a perfectly wetting, gravity-driven, thin, continuously-fed liquid film down an inclined planar substrate is modelled using the long-wave approximation with, as observed experimentally, a periodic pattern of finger-like rivulets forming at the unstable advancing front. The required long-time solution, with the merger of neighbouring rivulets a possibility, is obtained using a purpose designed efficient multigrid methodology incorporating complementary error-controlled automatic spatio-temporal adaptivity and mesh devolution strategies. Critical wavelengths are extracted from the various solutions showing the effect of inclination angle and comparison drawn with the results of a linear stability analysis (LSA) based on the same flow conditions.

Keywords: Multigrid, spatio-temporal adaptation, rivulets, lubrication theory.

1 Introduction

The motion of a thin liquid film down an inclined planar substrate can result in complex behaviour and interesting dynamics at the associated advancing front which becomes unstable, forming a periodic pattern of finger shaped rivulets. Huppert's [1] first detailed study of the problem showed the critical wavelength of the emerging instability, when scaled with the capillary length of the fluids considered, to be captured by a single linear fit of the data collected. This inspired many subsequent investigations including several experimental ones, see for example [2, 3, 4], the results of which were found to be in broad agreement with his findings.

In the intervening years, theoretical investigations have concentrated, in the main, on linear stability analyses of the travelling wave solution, see [5]; this approach does, however, prove inadequate for substrates with a low inclination angle. An alternative approach is to explore the full three-dimensional problem [6], requiring a numerical solution of the associated governing equations. This route is adopted here by invoking the simplifying assumption that the flow can be considered lubrication like [7].

To fully resolve the advancing front requires a fine computational grid and thus an efficient numerical method is necessary to obtain long-time solutions. Multigrid methods have been developed for use with lubrication type film flows on non-planar substrate featuring topographies and occlusions; within these methods automatic error-controlled local mesh refinement and time-stepping has been included to improve efficiency [7, 8]. Li *et al.*[9] developed a shifting mesh algorithm specifically to allow for the investigation of long-time rivulet formation, taking advantage of the large areas of constant film thickness in the problem, but it is restrictive in the sense that it is not suitable for use with automatic, error-controlled local mesh refinement. Accordingly a different grid devolution strategy is used in the present work.

2 Problem Formulation

The problem of interest is shown schematically in Figure 1. It consists of a thin fluid film of thickness H , flowing down a substrate (width, W_p , length, L_p) inclined at angle θ to the horizontal; the volumetric flow

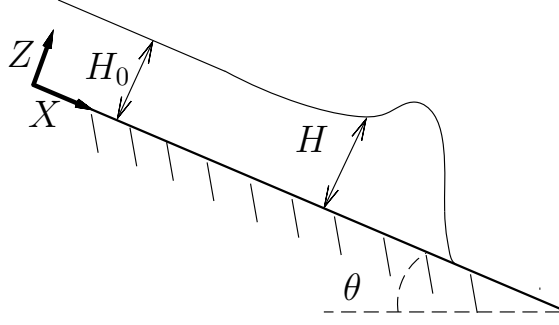


Figure 1: Schematic diagram of the cross-sectional film flow down a planar substrate (width, W_p , length, L_p) inclined at an angle α to the horizontal. H_0 denotes the asymptotic, fully-developed film thickness and H the film thickness at any (x, y) point.

rate is Q_0 per unit width. The fluid is considered to be incompressible with constant density, ρ , viscosity, μ , and surface tension, σ and to be perfectly wetting. A precursor film of thickness, H^* ($\ll H_0$), located ahead of the advancing front [5, 6, 10]. The long wave approximation is invoked on the assumption that the asymptotic film thickness, H_0 , is small compared to the capillary length, $L_0 = H_0/(6Ca)^{1/3}$, where $Ca = \mu U_0/\sigma \sim O(\epsilon^3) \ll 1$ is the capillary number, that is $H_0/L_0 = \epsilon \ll 1$. Taking the characteristic velocity as $U_0 = 3Q_0/2H_0$, and introducing the following scalings [8]:

$$(x, y) = \frac{(X, Y)}{L_0}, \quad z = \frac{Z}{H_0}, \quad h(x, y, t) = \frac{H(X, Y, T)}{H_0}, \quad t = \frac{U_0 T}{L_0},$$

$$p(x, y, z, t) = \frac{2P(X, Y, Z, T)}{\rho g L_0 \sin \theta}, \quad (u, v, w) = \left(\frac{U}{U_0}, \frac{V}{U_0}, \frac{W}{\epsilon U_0} \right), \quad h^* = \frac{H^*}{H_0},$$

the governing Navier-Stokes and continuity equations, for no slip at the substrate and the usual stress and kinematic conditions at the free surface [11], reduce to the following coupled equation set:

$$\frac{\partial h}{\partial t} = \frac{\partial}{\partial x} \left[\frac{h^3}{3} \left(\frac{\partial p}{\partial x} - 2 \right) \right] + \frac{\partial}{\partial y} \left[\frac{h^3}{3} \left(\frac{\partial p}{\partial y} \right) \right], \quad (1)$$

$$p = -\frac{\epsilon^3}{Ca} \nabla^2 h + 2\epsilon (h - z) \cot \theta, \quad (2)$$

where h and p are the non-dimensional film height and pressure, respectively.

At the upstream boundary a fully developed film thickness is prescribed ($h = 1$) while the downstream boundary is set such that $h(l_p, y) = h^*$ with zero flux conditions defined for h and p at the other boundaries, namely:

$$\left. \frac{\partial h}{\partial x} \right|_{x=0} = \left. \frac{\partial p}{\partial x} \right|_{x=0} = \left. \frac{\partial h}{\partial x} \right|_{x=l_p} = \left. \frac{\partial p}{\partial x} \right|_{x=l_p} = 0,$$

$$\left. \frac{\partial p}{\partial y} \right|_{y=0} = \left. \frac{\partial p}{\partial y} \right|_{y=w_p} = \left. \frac{\partial h}{\partial y} \right|_{y=0} = \left. \frac{\partial h}{\partial y} \right|_{y=w_p} = 0.$$

where $l_p = L_p/L_0$ and $w_p = W_p/L_0$. The initial film profile consists of a front perturbed with a superposition of N modes with random length, $l_j \in [-0.2, 0, 2]$, and differing wavelength, $\lambda_{0,j}$, as in [6] via:

$$h(x, y) = 0.5 \left\{ 1 + h^* - (1 - h^*) \tanh \left[\frac{(x - x_f(y))}{\delta} \right] \right\}, \quad (3)$$

$$x_f(y) = x_u - \sum_{j=1}^M l_j \cos(2\pi y/\lambda_{0,j}), \quad (4)$$

where x_u is the position of the slope of the unperturbed front (a value of 30 is prescribed); δ is the steepness of the profile (taken to be 0.01) and $\lambda_{0,j} = 2w_p/j$ for $j = 1, \dots, M$. The results are independent of the initial condition provided M is sufficiently large - a value of $M = 50$ is found to be adequate.

3 Method of solution: adaptive multigrid

Given the extent of the solution domain involved and the long-time solutions required, a key feature of the numerical methodology used to solve equations (1) and (2), is one based on a strategy employing automatic error controlled adaptive time stepping and mesh refinement within an efficient multigrid framework as described below. Noting that sufficiently far away from the advancing front, the film thickness remains constant, provides another avenue for exploitation, in that judiciously removing nodes in such regions has a dramatic effect in terms of further reducing the solution time without loss of accuracy.

3.1 Spatial discretisation

Discrete forms of equations (1) and (2) were obtained using central-differencing [8], leading to second order accurate spatial analogues of the form:

$$\frac{\partial h_{i,j}}{\partial t} = \frac{1}{\Delta^2} \left[\frac{h^3}{3} \Big|_{i+\frac{1}{2},j} (p_{i+1,j} - p_{i,j}) - \frac{h^3}{3} \Big|_{i-\frac{1}{2},j} (p_{i,j} - p_{i-1,j}) \right. \\ \left. + \frac{h^3}{3} \Big|_{i,j+\frac{1}{2}} (p_{i,j+1} - p_{i,j}) - \frac{h^3}{3} \Big|_{i,j-\frac{1}{2}} (p_{i,j} - p_{i,j-1}) \right] \\ - \frac{2}{\Delta} \left(\frac{h^3}{3} \Big|_{i+\frac{1}{2},j} - \frac{h^3}{3} \Big|_{i-\frac{1}{2},j} \right), \quad (5)$$

$$p_{i,j} + \frac{\epsilon^3}{Ca\Delta^2} [h_{i+1,j} + h_{i-1,j} + h_{i,j+1} + h_{i,j-1} - 4h_{i,j}] - 2\epsilon h_{i,j} \cot \theta = 0, \quad (6)$$

for all points (i, j) in the computational domain, Ω ; with Δ the grid size (for simplicity a square mesh is employed). The prefactors in equation (5) are obtained using linear interpolation between neighbouring grid points and are given by, for example,

$$\frac{h^3}{3} \Big|_{i+\frac{1}{2},j} = \frac{1}{2} \left(\frac{1}{3} h_{i+1,j}^3 + \frac{1}{3} h_{i,j}^3 \right),$$

and similarly defined for the other prefactors.

3.2 Temporal discretisation

Equation (1) is discretised temporally using the implicit, second-order accurate Crank-Nicolson method to approximate the time derivatives involved in equation (5). For convenience the spatial discretisation is written as a function of $h_{i,j}, p_{i,j}, h_{i\pm 1,j}$ and $p_{i\pm 1,j}$ so that:

$$\frac{\partial h_{i,j}}{\partial t} = F(h_{i,j}^n, p_{i,j}^n, h_{i\pm 1,j}^n, p_{i\pm 1,j}^n, h_{i,j\pm 1}^n, p_{i,j\pm 1}^n) \quad (7)$$

for all $(i, j) \in \Omega$. Employing the Crank-Nicolson method yields an equation for the variables h and p at t^{n+1} (denoted by superscript $n+1$) in terms of the calculated values at $t = t^n$ (denoted by superscript n), namely:

$$h_{i,j}^{n+1} - \frac{\Delta t^{n+1}}{2} F(h_{i,j}^{n+1}, p_{i,j}^{n+1}, h_{i\pm 1,j}^{n+1}, p_{i\pm 1,j}^{n+1}, h_{i,j\pm 1}^{n+1}, p_{i,j\pm 1}^{n+1}) \\ = h_{i,j}^n + \frac{\Delta t^{n+1}}{2} F(h_{i,j}^n, p_{i,j}^n, h_{i\pm 1,j}^n, p_{i\pm 1,j}^n, h_{i,j\pm 1}^n, p_{i,j\pm 1}^n), \quad (8)$$

with $\Delta t^{n+1} = t^{n+1} - t^n$.

3.3 Full multigrid strategy

The advantage of multigridding is the ability to solve a problem having N unknowns in $O(N)$ operations [8]. The multigrid solver employed incorporates a Full Approximation Storage (FAS) algorithm that makes use of the solution calculated on coarser grids to reduce the error on finer grids; the FAS algorithm is coupled with a full multigrid (FMG) technique, designed to avoid possible divergence due to a poor initial solution [8]. The succession of finer grids employed, denoted by \mathcal{G}_k (with $k = 0, 1, 2, \dots, K$), span the solution domain; the number of nodes in the x and y -coordinate directions on grid \mathcal{G}_k is given by $n_k = A_x 2^k + 1$ with $m_k = A_y 2^k + 1 + 1$, respectively, where A_x and A_y are prescribed constants.

The multigrid efficiency of the solution strategy is improved further by implementing automatic error-controlled grid refinement [8] where only areas of highest error are resolved on finer grids. Variable time stepping is also utilised by estimating the maximum local truncation error at each time iteration and using it to determine the size of the next time step; further details of how the local truncation error is calculated and employed can be found in Gaskell *et al.*[12].

3.3.1 Grid devolution

While the method of solution described above is particularly streamlined for the problem of continuous film flow, there is the possibility of improving the efficiency further when considering the long-time evolution of an advancing front, since large areas of the computational domain have a known constant film thickness. One approach is to devolve the solution grid in regions where there is no perceptible change in the film profile; this is particularly suitable for the consideration of rivulet growth since downstream of the advancing front the thickness of the precursor film is just h^* ($\ll 1$) while upstream of it the film is fully developed, that is $h = 1$. Using this knowledge a criteria for devolution can be constructed based on the gradient of the solution at the grid devolution start level, \mathcal{G}_d (in the work reported here \mathcal{G}_d is taken as \mathcal{G}_0). Should the gradient be smaller than a specified tolerance then the node is marked for devolution and is excluded from subsequent calculations for the current time iteration. This creates a dynamically changing computational domain that is sufficiently large to capture the non-linear behaviour at the advancing front but much smaller than the original domain size.

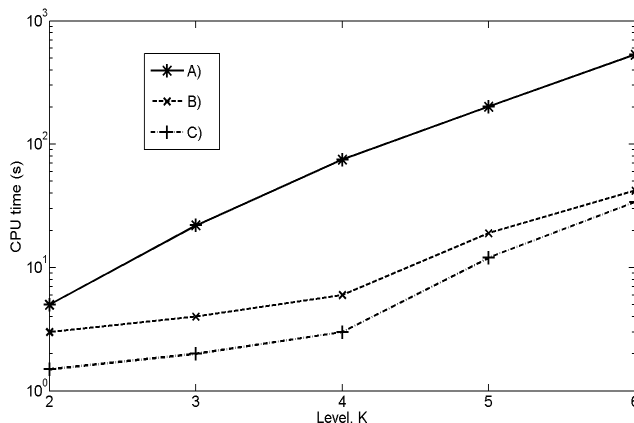


Figure 2: The CPU time for a typical time iteration with finest grid \mathcal{G}_K , shown for three different adaption strategies: A) no mesh adaption, B) local mesh refinement and C) local mesh refinement together with grid devolution. This is for ‘Fluid A’ [4] flowing down a substrate inclined at 60° to the horizontal; the coarsest grid \mathcal{G}_0 contains 129×65 nodes and the computational domain is $(0, 200) \times (0, 100)$.

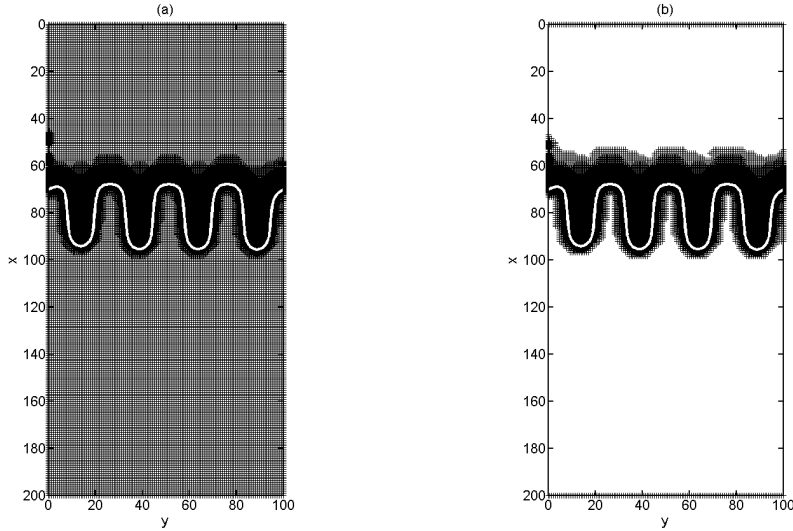


Figure 3: The refined grid structure used in the multigrid solution of thin film flow for a fully wetting liquid spreading on an inclined substrate with $\alpha = 60^\circ$ when adaption strategies B), shown in (a), and C), shown in (b), are utilised. The contact line is indicated in white.

4 Results

Results were generated for a liquid having the same properties as ‘Fluid A’ from Johnson *et al.* [4], a water-glycerin mixture; that is with density, $\rho = 1075 \text{ kg m}^{-3}$, viscosity, $\mu = 3.11 \times 10^{-2} \text{ Pa s}$ and surface tension, $\sigma = 0.069 \text{ Pa m}$. The flow rate is $Q_0 = 0.29 \text{ mm}^2/\text{s}$ which for inclination angle 50° gives $H_0 = 0.7 \text{ mm}$. The fluid is perfectly wetting and the value of the precursor film, h^* , is taken as 0.01 [6].

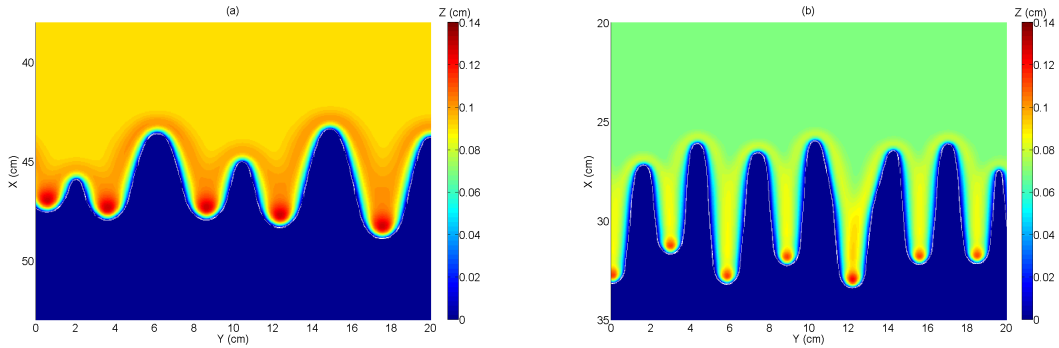


Figure 4: Free surface colour maps of film thickness for film flow down a substrate inclined at (a) 20° and (b) 50° . Note the shift in the x-axis to keep the advancing front central.

4.1 Adaptive multigrid efficiency

Solutions were found for the case of a perfectly wetting liquid film flowing down on a rigid substrate inclined at $\alpha = 60^\circ$ to the horizontal, the computational domain being $\Omega = (0, 200) \times (0, 100)$. G_0 contained 129×65 nodes, so $n_k = 128 \times 2^k + 1$ and $m_k = 64 \times 2^k + 1$; the finest grid was \mathcal{G}_K , with local mesh refinement active from \mathcal{G}_2 . The CPU time for a typical full multigrid time iteration is shown in Figure 2 corresponding

to three different adaption strategies: A) no mesh adaption, B) local mesh refinement and C) local mesh refinement together with grid devolution. Figure 2 shows that B) results in a large reduction in CPU time, an order of magnitude difference compared to A), as the refined region involving finer mesh levels contains many fewer nodes than an equivalent full grid spanning the entire solution domain. A further enhancement in efficiency is obtained by employing option C); the removal of unnecessary nodes on all grid levels spanning the full solution domain is found to save as much as 50% more CPU time per time iteration. This further improvement is enabled because the number of calculations performed on coarser levels is vastly reduced.

The corresponding evolving flow pattern obtained with adaption strategies B) and C) is shown for comparison purposes in Figure 3 (a) and (b), respectively; the contact line is delineated in white. Note how the grid refines in the region of the advancing front and devolves away from the area of interest. When strategy A) is employed the full solution grid contains 525,825 nodes. For the grid shown in Figure 3 (a), strategy B), the number of nodes has been reduced to 77,942; when grid devolution is employed in tandem, strategy C), this number reduces further to 49,098, see Figure 3 (b), demonstrating quite effectively the improved efficiency obtained. Grid devolution essentially decreases the size of the active computational domain; in Figure 3 (b) the effective size of this domain is approximately 10% of the original whole.

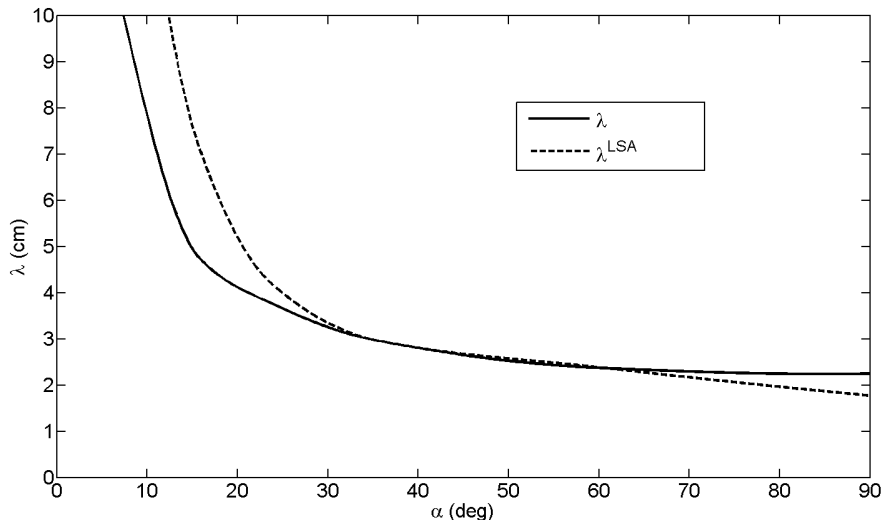


Figure 5: Wavelength, λ , for the rivulet pattern at the advancing front of a spreading perfectly wetting thin film as extracted from the numerical solutions. Results calculated from a LSA, λ_{LSA} , are shown for comparison purposes.

4.2 Long time rivulet evolution

Figure 4 shows free surface colour maps of the rivulet pattern at the advancing front of a thin liquid film for two different inclination angles; 20° and 50° . The plots highlight the differences that result from the change in inclination angle; for instance the rivulets when $\alpha = 50^\circ$ are thinner, they are also more elongated [13]. Also worth noting is the change in shape between the different scenarios, at the lower inclination angle the advancing front is more saw-tooth shaped, as the inclination angle is increased the rivulets become thin and more finger-like.

The wavelength, λ , varies in accordance with the width of the rivulets; wavelength is measured as the average distance between the tips of adjacent rivulets across the advancing front. There are a higher number of rivulets, thus a smaller wavelength, at high inclination angles; the rivulets are wider at lower inclination angles and the wavelength lengthens. Figure 5 shows the wavelength extracted from numerical solutions for a range of inclination angles up to the vertical. For comparison purposes, the result associated with a corresponding linear stability analysis (LSA), derived as in [5], is also plotted on Figure 5. The predicted

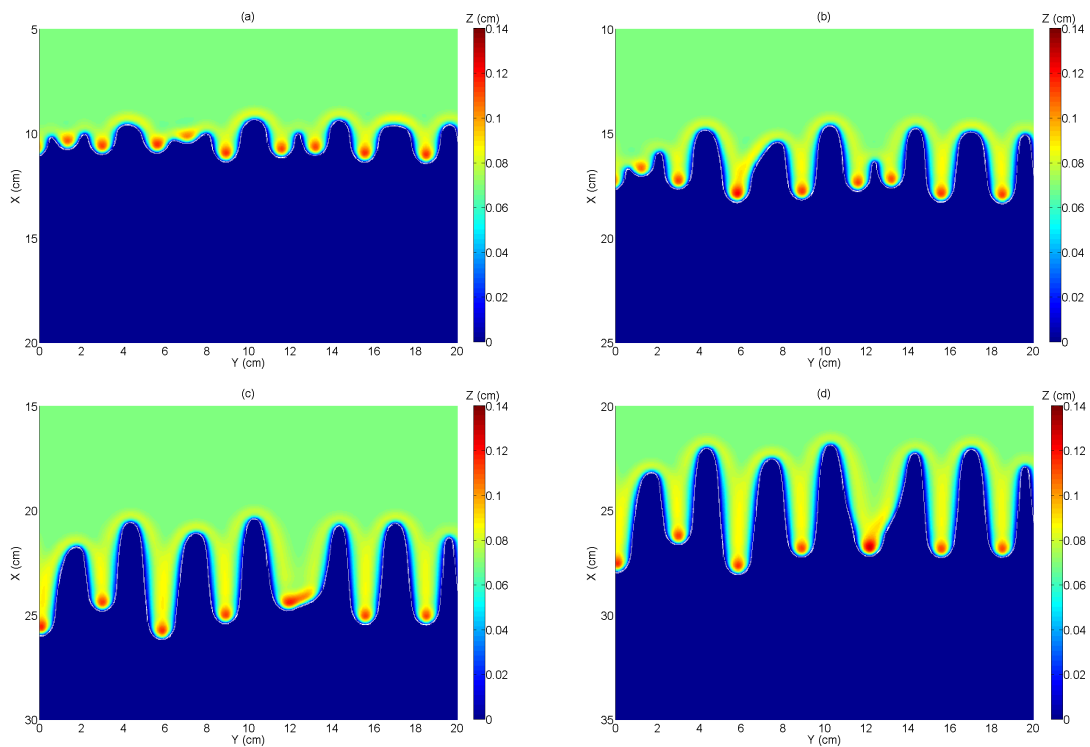


Figure 6: Free surface colour maps of film flow down a substrate inclined at 50° showing the evolution of the advancing front, at four different instants of time. Note the shift in axis position to keep the rivulets in central view.

wavelength from the LSA, λ^{LSA} , is calculated from the fastest growing wavenumber; while there is reasonable agreement at high inclination angles the same is much less favourable at low values of α .

During the evolution of the advancing front neighbouring rivulets show a tendency to merge into one another if they form in close proximity; this is clearly demonstrated for the evolution of the advancing front in Figure 6. The shape and dynamics of the rivulet pattern changes as it advances; merging rivulets accelerate ahead of the bulk of the flow as the capillary ridge, a characteristic feature of an advancing front, increases in height leading to a faster growing rivulet.

5 Conclusion and Future Work

The advancing front of a perfectly wetting thin liquid film spreading on a rigid, inclined substrate develops rivulets that grow ahead of the bulk of the fluid, the dynamics of which are considered computationally via an efficient multigrid method of solution that incorporates automatic, error-controlled local mesh refinement and time-stepping. The method is further enhanced by the introduction of a complementary grid devolution strategy. As a whole the methodology is found to be well suited to generating long-time solutions of the associated problem.

Numerical results revealed the effect of inclination angle on long-time rivulet formation; the shape, length and width of the rivulets all depending on the steepness of the substrate. An interesting feature of the flow, the coalescence of neighbouring rivulets, is also observed.

The robustness of the solution strategy provides the opportunity to extend it to problems involving additional physical effects or a parameter range that would be significantly more difficult to control in an experimental environment, such as the case of a partially wetting liquid or the introduction of surface tension gradients.

References

- [1] H. E. Huppert. Flow and instability of a viscous current down a slope. *Nature*, 300(5891):427–9, 1982.
- [2] N. Silvi and E. B. Dussan V. The rewetting of an inclined solid surface by a liquid. *Physics of Fluids*, 28, 1985.
- [3] J. M. Jerrett and J. R. de Bruyn. Fingering instability of a gravitationally driven contact line. *Physics of Fluids A*, 4, 1992.
- [4] M. F. G. Johnson, R. A. Schluter, M. J. Miksis, and S. G. Bankoff. Experimental study of rivulet formation on an inclined plate by fluorescent imaging. *Journal of Fluid Mechanics*, 394:339–354, 1999.
- [5] A. L. Bertozzi and M. P. Brenner. Linear stability and transient growth in driven contact lines. *Physics of Fluids*, 9(3):530–9, 1997.
- [6] L. Kondic and J. Diez. Pattern formation in the flow of thin films down an incline: Constant flux configuration. *Physics of Fluids*, 13(11):3168–3184, 2001.
- [7] M. Sellier H. M. Thompson P. H. Gaskell, P. K. Jimack and M. C. T. Wilson. Efficient and accurate time adaptive multigrid simulations of droplet spreading. *Journal of Fluid Mechanics*, 509:253–280, 2004.
- [8] Y. C. Lee, H. M. Thompson, and P. H. Gaskell. An efficient adaptive multigrid algorithm for predicting thin film flow on surfaces containing localised topographic features. *Computers and Fluids*, 36:838–855, 2007.
- [9] Yibao Li, Hyun Geun Lee, Daeki Yoon, Woonjae Hwang, Suyeon Shin, Youngsoo Ha, and Junseok Kim. Numerical studies of the fingering phenomena for the thin film equation. *International Journal for Numerical Methods in Fluids*, 67(11):1358–1372, 2011.
- [10] Y. Zhao and J. S. Marshall. Dynamics of driven liquid films on heterogeneous surfaces. *Journal of Fluid Mechanics*, 559:355–378, 2006.
- [11] S. Veremieiev, H. M. Thompson, Y. C. Lee, and P. H. Gaskell. Inertial thin film flow on planar surfaces featuring topography. *Computers and Fluids*, 39(3):431–450, 2010.
- [12] P. H. Gaskell, P. K. Jimack, M. Sellier, and H. M. Thompson. Efficient and accurate time adaptive multigrid simulations of droplet spreading. *International Journal for Numerical Methods in Fluids*, 45:1161–1186, 2004.
- [13] L. Kondic and J. A. Diez. On nontrivial traveling waves in thin film flows including contact lines. *Physica D: Nonlinear Phenomena*, 209(1-4):135–144, 2005.